Electronic supplementary information

Tailoring the ternary synergistic effect of TBAH/H_2O/DMSO for room-temperature and ultrafast cellulose dissolution

*Jianan Zhu [a], Hao Sun [a, *], Jianrong Mao [a], Yuan Zou [a], Fulin Yang [a], Yunwu Zheng [a], Can Liu [a], Xu Lin [a], Defa Hou [a, *], Mingbo Yang [b *]*

a National Joint Engineering Research Center for Highly-Efficient Utilization Technology of Forestry Resource, Yunnan Provincial Key Laboratory of Wood and Bamboo Biomass Materials, Southwest Forestry University, Kunming 650224, P. R. China

b College of Polymer Science and Engineering, Sichuan University, Chengdu 610065, P. R. China

** To whom correspondence should be addressed. Email: yangmb@scu.edu.cn (Mingbo Yang), houdefa001@163.com (Defa Hou), and sunhao@swfu.edu.cn (Hao Sun).*

Contents

1. Supplementary experimental section

1.1 Preparation of TBAH/DMSO solution

To obtain TBAH/DMSO solution (50/50, w/w) without water (or with a slight amount of water), 100.0 g TBAH solution (40 wt.% in methanol, Adamas) was dissolved into 40.0 g DMSO (Safedry, Water ≤ 50 ppm, 99.7%, Adamas). Then, the transparent TBAH/methanol/DMSO solution was subjected to removing methanol by rotary evaporation (40 °C, > 8 h). The obtained TBAH/DMSO solution (50/50, w/w) was stored in sealed reagent bottles containing molecular sieves 4A (balls with diameters of 3 ~ 5 mm, Greagent). On the other hand, according to the reported method [1], TBAH was obtained by drying the TBAH solution (40 wt.% in methanol, Adamas) through rotary evaporation (40 °C, > 8 h). After that, designated TBAH was dissolved into DMSO (Safedry, Water ≤ 50 ppm, 99.7%, Adamas) at room temperature to achieve a TBAH/DMSO solution (50/50 w/w).

1.2 Detailed procedures for determining Kamlet-Taft (K-T) parameters

The Kamlet-Taft (K-T) parameters of TBAH/H_2O/DMSO solvents were determined using Reichardt's dye (RD, M_w = 551.68 g/mol), 4-nitroaniline (NA, M_w = 138.12 g/mol), and *N*, *N*-diethyl-4-nitroaniline (DENA, M_w = 178.24 g/mol) as molecular probes [2–4]. Initially, NA, DENA, and RD were uniformly dissolved in methanol with concentrations of 3 mg/mL, 3 mg/mL, and 7 mg/mL, respectively. Subsequently, the dye solutions were transferred into 5 mL centrifuge tubes and dried in a vacuum oven at 40 °C for 48 h to remove methanol. After that, 3 mL of TBAH/H_2O/DMSO was added to the dried dyes, and the mixture was stirred until the dyes dissolved completely. Then, the dyed TBAH/H_2O/DMSO solvent was transferred into a quartz cuvette (1 cm × 1 cm), and its absorption spectrum was measured at room temperature (25 °C) using a UV-Vis spectrophotometer (UV-3600i Plus, Shimadzu). Notably, the maximum

absorbance of the absorption spectrum was controlled in the range of 0.4 to 2.0 by varying the concentration of dyes in the dyed TBAH/H_2O/DMSO. Finally, the hydrogen bond acidity (α), hydrogen bond basicity (β), and polarizability (π*) values of TBAH/H_2O/DMSO were calculated based on the measured results.

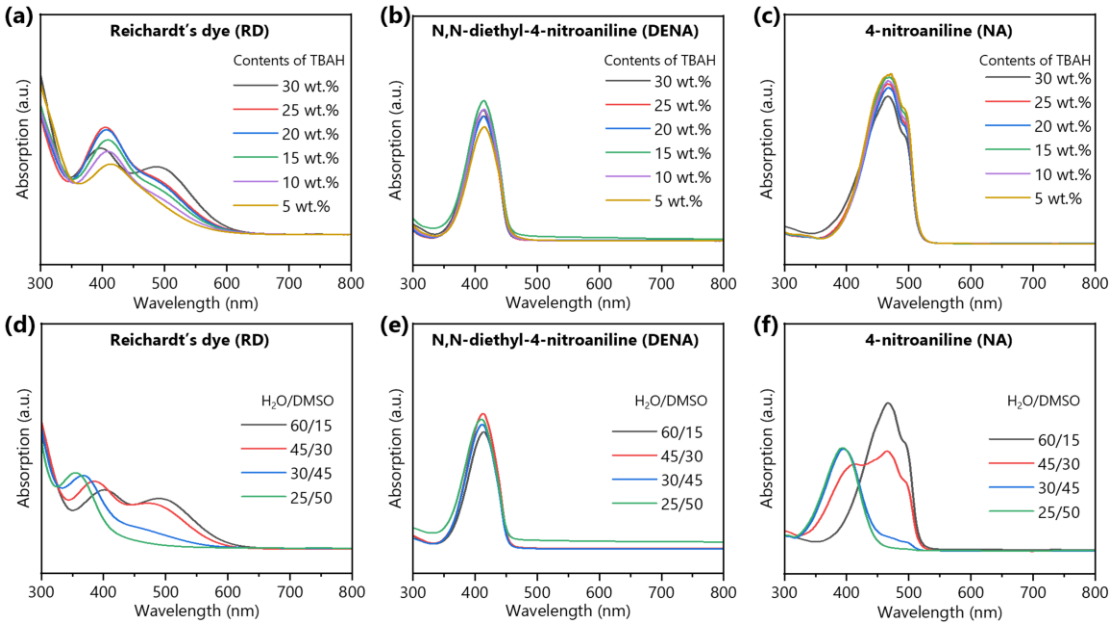

Figure S1 UV-Vis absorption spectra of various TBAH/H_2O/DMSO solvents dyed by molecular probes. (a-c) TBAH/H_2O/DMSO solvents with different TBAH concentrations (TBAH/H_2O = 1/1, w/w) that dyed by RD (a), DENA (b), and NA (c), respectively; (d-f) TBAH/H_2O/DMSO solvents with different concentrations of TBAH/H_2O (the concentration of TBAH was 25 wt.%) that dyed by RD (d), DENA (e), and NA (f), respectively.

1.3 Density functional theory (DFT) calculation

All DFT calculations were carried out using Gaussian 16 at the B3LYP/6-31G(d) level, including Grimme's D3(BJ) dispersion correction [5–8]. The gas-phase geometry optimizations and frequency analyses were performed to ensure that each stationary point corresponds to an actual minimum (no imaginary frequencies). Thermochemical parameters (enthalpy, entropy, and Gibbs free energy) were derived at 298.15 K and 1 bar using standard statistical thermodynamics. Based on wavefunctions obtained from

Gaussian 16 output files, the electrostatic potential (ESP) maps, van der Waals (vdW) maps, and reduced density gradient (RDG) isosurfaces of all samples (cellulose chain segment, TBAH, H_2O, and DMSO) were generated using Multiwfn 3.8(dev) [9–11]. Furthermore, the calculation results were visualized with VMD 1.9.3 [12]. Notably, the noncovalent interactions in different systems were identified via the sign(λ_2)ρ criterion.

1.4 Molecular dynamics simulation (MD)

Molecular dynamics (MD) simulations were performed with CP2K/Quickstep in the Gaussian–plane-wave (GPW) scheme (Born–Oppenheimer) under three-dimensional periodic boundary conditions [13]. Two cellulose oligomer chains (DP = 4) were solvated in an explicit TBAH/H_2O/DMSO solvent. Long-range electrostatics and boundary handling were treated with the periodic Poisson solver. The simulation boxes are summarized in Table S1 by lattice parameters **(**a, b, c, α, β, and γ**)** and volume.

Table S1 Detailed unit-cell parameters and volume of cellulose.

Stage	a (Å)	b (Å)	c (Å)	α (°)	β (°)	γ (°)	Volume (Å³)
Pre-MD orthorhombic (opt)	28.54	28.60	29.62	90	90	90	24183
MD triclinic (production)	28.44	27.84	29.55	88.89	87.81	87.80	23358

Electronic structure was described using the PBE exchange–correlation functional with Grimme D3(BJ) dispersion, Goedecker–Teter–Hutter (GTH-PBE) pseudopotentials, and DZVP-MOLOPT-SR-GTH basis sets for all elements [14–17]. The auxiliary plane-wave density expansion employed cut-offs of CUTOFF = 500 Ry and REL_CUTOFF = 50 Ry. Self-consistent optimization used the orbital-transformation scheme with a DIIS minimizer. The SCF convergence threshold was set to EPS_SCF = 1.0×10^{-6}, with up to 20 outer iterations per MD step. Wavefunctions were extrapolated with the

always-stable predictor–corrector (ASPC) method (order 3). Spin polarization was not employed.

Prior to dynamics, variable-cell geometry optimization was carried out at 1 bar using analytical stress evaluation (DIRECT_CELL_OPT). This procedure relaxed both the atomic positions and the lattice vectors. Production trajectories was obtained followed a two-stage protocol: (i) canonical (NVT) dynamics was performed at 298.15 K for 2 000 steps with a time step of Δt = 1.0 fs, in which the temperature was controlled by the canonical sampling through velocity rescaling thermostat (CSVR; τ_t = 200 fs); (ii) isothermal–isobaric dynamics with an isotropic barostat (NPT_I) was performed at 298.15 K and 1 bar for 6000 steps using the same CSVR thermostat (τ_t= 200 fs) with a barostat time constant of τ_p = 1 000 fs. Atomic coordinates were written at every MD step in DCD format, and restart files (coordinates, velocities and CP2K restart records) were synchronized with the trajectory output to enable seamless continuation. The post-processing of trajectory was carried out using GROMACS 2020 and visualized in VMD 1.9.3 [18, 19].

2 Dissolution of cellulose in TBAH/H_2O/DMSO solvents

2.1 Effect of TBAH/H_2O/DMSO dissolution on the crystalline structure of MCC

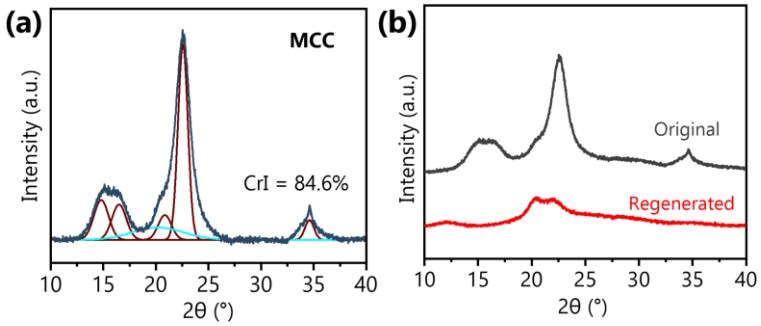

Figure S2 XRD patterns of MCC and the corresponding regenerated cellulose.

According to the XRD patterns of MCC and the corresponding regenerated cellulose, it was found that MCC with cellulose I (2θ = 15.1°, 16.3°, and 22.4°) crystals was transformed into cellulose II crystals (2θ =20 - 22°) after TBAH/H_2O/DMSO dissolution [20]. This result suggested the complete dissolution of MCC in TBAH/H_2O/DMSO solvent.

2.2 Chemical structures of MCC and the corresponding regenerated cellulose

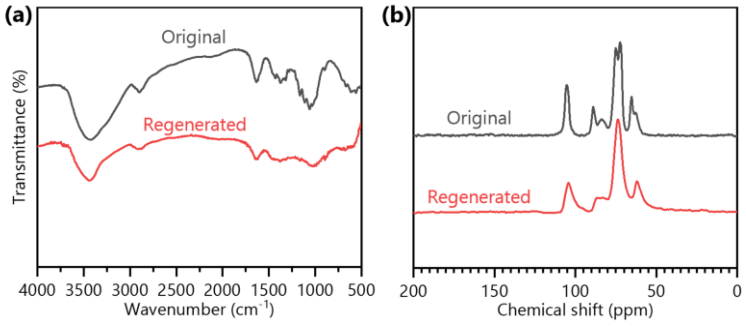

Figure S3 FT-IR (a) and solid-state ^{13}C CP/MAS NMR (b) spectra of MCC and the corresponding regenerated cellulose.

As shown in Figure S3, MCC and the corresponding regenerated cellulose showed

similar FT-IR and ^{13}C NMR spectra, suggesting their similar chemical structure. Moreover, in the FT-IR spectra of MCC and the corresponding regenerated cellulose, similar O–H bonds (3380–3470 cm^{-1}) and C–H bonds (2897 cm^{-1}) absorption was observed. Meanwhile, compared with MCC, the bending absorption of C-H bonds (1367 cm^{-1}) was weakened in the FT-IR spectrum of the regenerated cellulose, indicating partial loss of O_6–H···O_3 hydrogen bonds. Besides, in the FT-IR spectrum of the regenerated cellulose, a blue shift and a reduced intensity of O–H bonds characteristic absorption were detected, suggesting the crystallinity of cellulose decrease [21]. A similar result was also found in CP/MAS^{13}C NMR characterization, evident downfield shifts of C4 and C6 (89 ppm to 82 ppm and 65 ppm to 61 ppm) were observed, confirming the conversion of cellulose I into cellulose II [22]. Thus, the FT-IR and ^{13}C NMR analysis also confirmed the complete dissolution of MCC in TBAH/H_2O/DMSO solvent.

2.3 Solubility of MCC in TBAH/H_2O and TBAH/H_2O/DMSO solvents

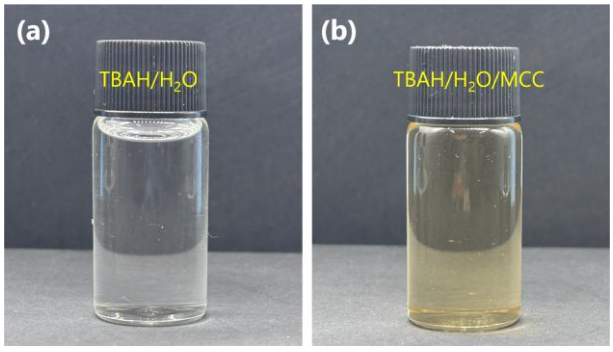

Figure S4 Digital images of TBAH/H_2O (50/50, w/w) solution (a) and TBAH/H_2O/MCC (50/50/4, w/w/w) solution (b).

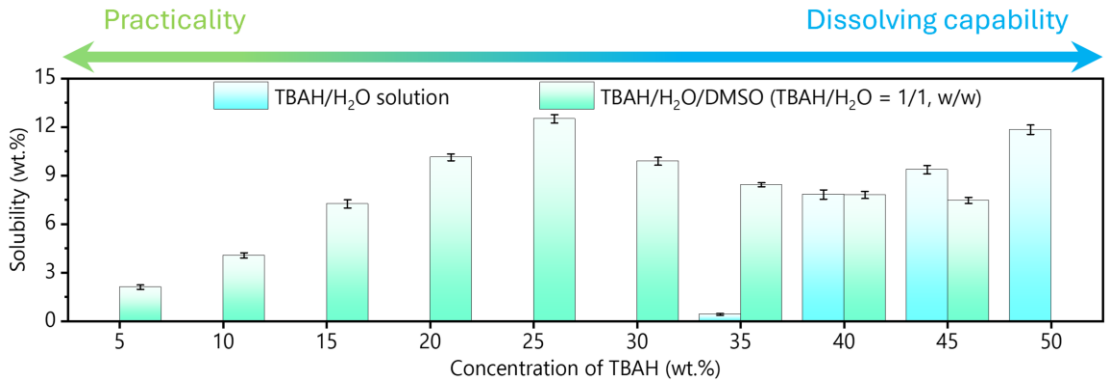

Figure S5 Solubility of MCC in TBAH/H_2O and TBAH/H_2O/DMSO (TBAH/H_2O = 1/1, w/w) with different TBAH concentration via a one-step strategy.

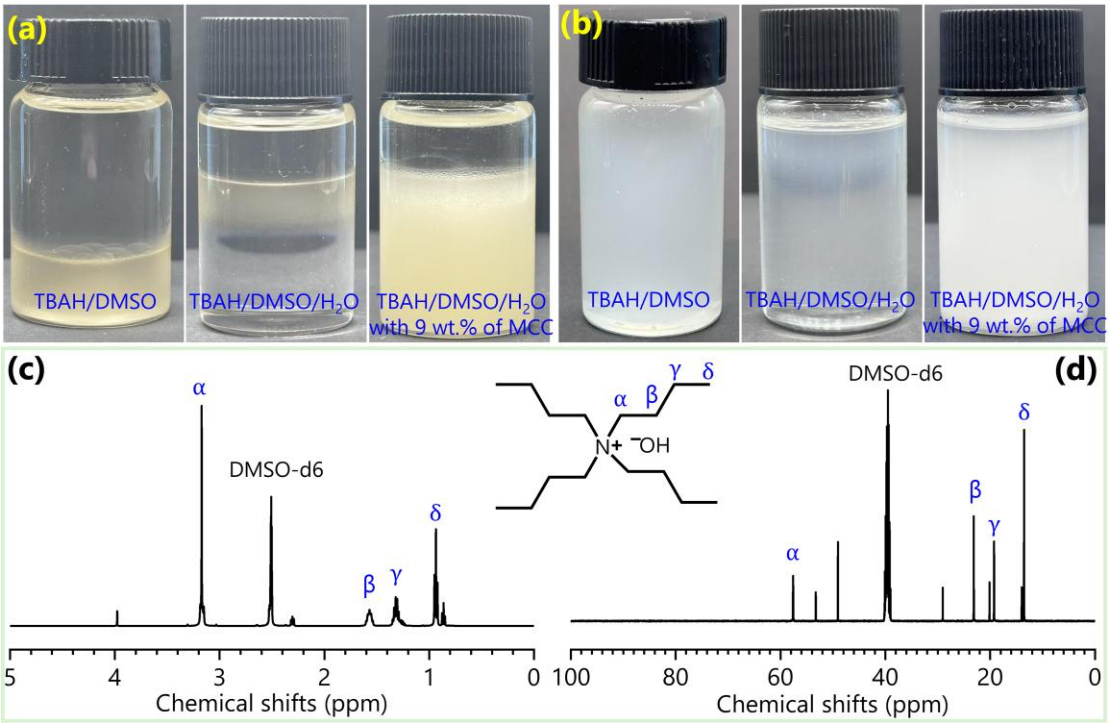

Figure S6 Preparation and characterization of TBAH. (a, b) Digital images of TBAH/DMSO (25/75, w/w) solution obtained by evaporating TBAH/H_2O solution (a) and TBAH/methanol/DMSO solution (b); ^{1}H NMR (c) and ^{13}C NMR (d) of TBAH obtained by evaporating TBAH/H_2O solution.

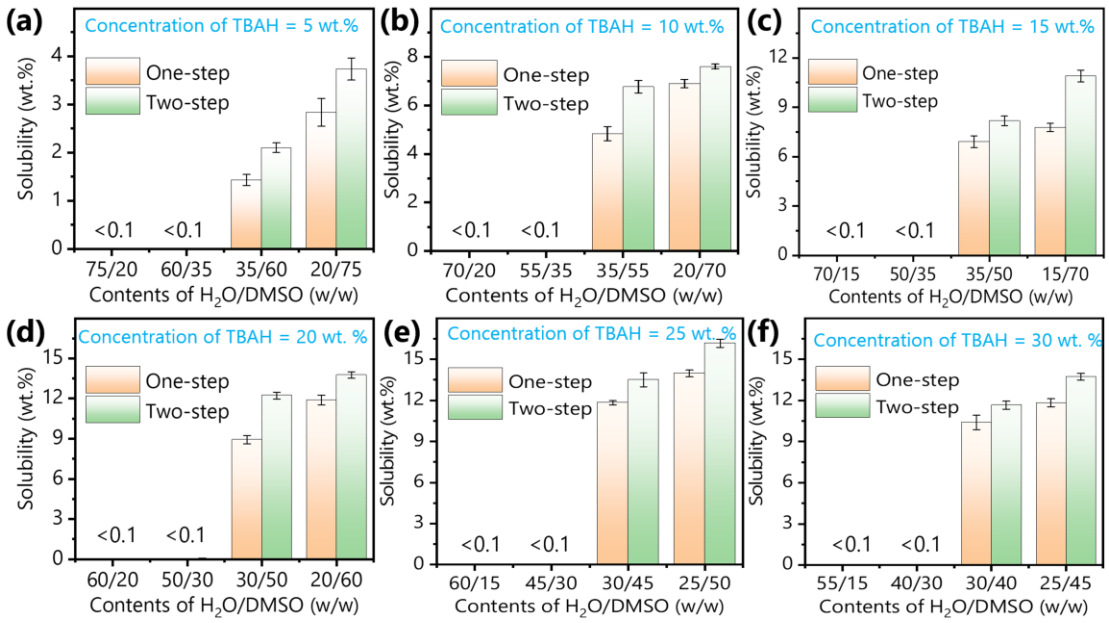

Figure S7 Solubility of MCC in various TBAH/H_2O/DMSO as the TBAH concentration and the contents of H_2O/DMSO were tuned.

Table S2 Detailed protocols for using TBAH/H_2O/DMSO to dissolve cellulose (unit: wt.%).

Solvents	Formulation			Solubility	
	TBAH	H_2O	DMSO	One-step	Two-step
$B_5H_{95}S_0$	5	95	0	0	0
$B_5H_{76}S_{19}$		76	19	0	0
$B_5H_{57}S_{38}$		57	38	0	0
$B_5H_{38}S_{57}$		38	57	1.5	2.1
$B_5H_{19}S_{76}$		19	76	2.8	3.7
$B_{10}H_{90}S_0$	10	90	0	0	0
$B_{10}H_{72}S_{18}$		72	18	0	0
$B_{10}H_{54}S_{36}$		54	36	0	0
$B_{10}H_{36}S_{54}$		36	54	4.8	6.8
$B_{10}H_{18}S_{72}$		18	72	6.9	7.6
$B_{15}H_{85}S_0$	15	85	0	0	0
$B_{15}H_{68}S_{17}$		68	17	0	0
$B_{15}H_{51}S_{34}$		51	34	0	0
$B_{15}H_{34}S_{51}$		34	51	6.9	8.2
$B_{15}H_{17}S_{68}$		17	68	7.8	10.9
$B_{20}H_{80}S_0$	20	80	0	0	0
$B_{20}H_{64}S_{16}$		64	16	0	0
$B_{20}H_{48}S_{32}$		48	32	0	0
$B_{20}H_{32}S_{48}$		32	48	8.9	12.2
$B_{20}H_{16}S_{64}$		16	64	11.9	13.8
$B_{25}H_{75}S_0$	25	75	0	0	0
$B_{25}H_{60}S_{15}$		60	15	0	0
$B_{25}H_{45}S_{30}$		45	30	0	0
$B_{25}H_{30}S_{45}$		30	45	11.8	13.5
$B_{25}H_{15}S_{60}$		15	60	14.0	16.2
$B_{30}H_{70}S_0$	30	70	0	0	0
$B_{30}H_{56}S_{14}$		56	14	0	0
$B_{30}H_{42}S_{28}$		42	28	0	0
$B_{30}H_{28}S_{42}$		28	42	10.4	11.7
$B_{30}H_{14}S_{56}$		14	56	11.8	13.7

2.4 Dissolution of various cellulose in TBAH/H_2O/DMSO solvent

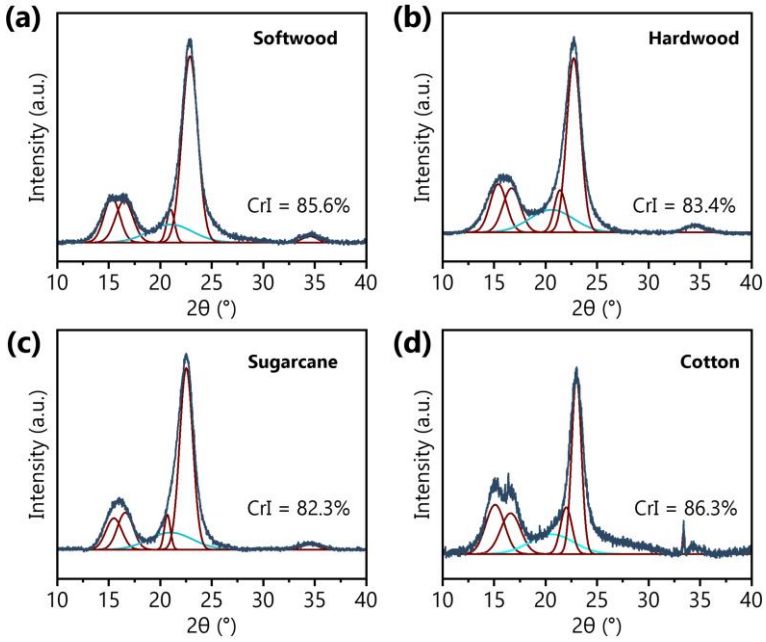

Figure S8 XRD fitting patterns of various cellulose analyzed by Gaussian peak fitting. (a) Softwood pulp; (b) Hardwood pulp; (c) Sugarcane pulp; (d) Cotton pulp.

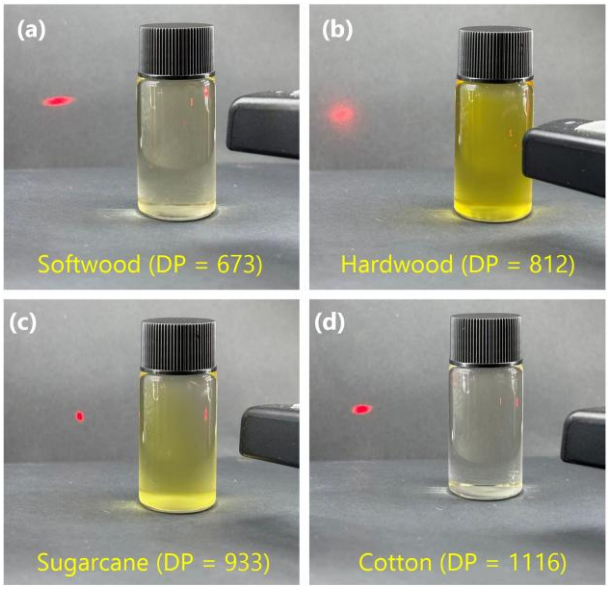

Figure S9 Digital images of various cellulose solution with a concentration of 2 wt.% obtained by TBAH/H_2O/DMSO dissolution. (a) Softwood pulp; (b) Hardwood pulp; (c) Sugarcane pulp; (d) Cotton pulp.

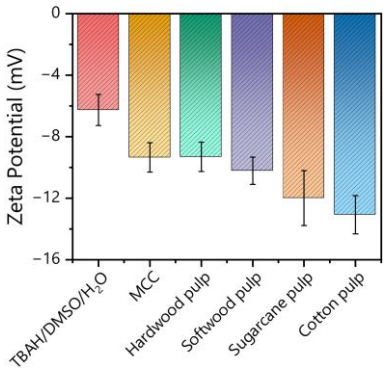

Figure S10 Zeta potential of TBAH/H_2O/DMSO solvent and various cellulose solution obtained by TBAH/H_2O/DMSO dissolution.

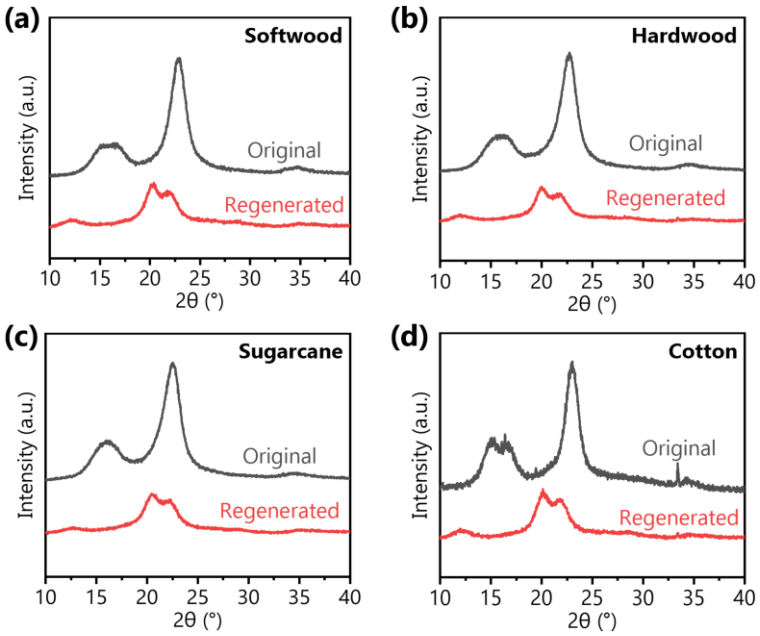

Figure S11 XRD patterns of various cellulose and the corresponding regenerated cellulose. (a) Softwood pulp; (b) Hardwood pulp; (c) Sugarcane pulp; (d) Cotton pulp.

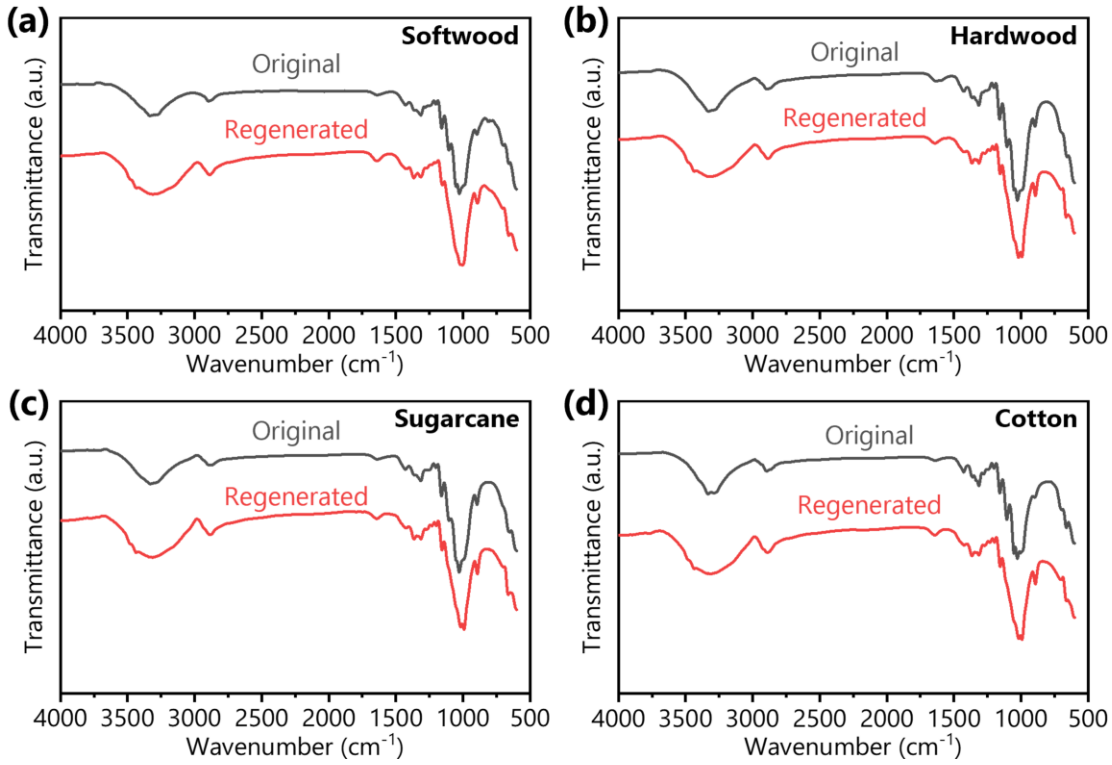

Figure S12 FT-IR spectra of various cellulose and the corresponding regenerated cellulose. (a) Softwood pulp; (b) Hardwood pulp; (c) Sugarcane pulp; (d) Cotton pulp.

2.5 Comparison of TBAH/H_2O/DMSO with conventional cellulose solvents

Table S3 Comparison of dissolution performance of this work with conventional studies [23–31].

Solvent type	Solvent temperature(°C)	Dissolution time	Solubility (wt.%)	Max DP	Moisture sensitivity
NMMO	90 – 120	10 – 60 min	8 – 20	800 – 1000	High
DMAc/LiCl	80 – 120	24 h	3 – 8	1800	High
[EMIM][OAc]	70 – 120	15 min	1 – 20	4000	High
NaOH/H_2O/urea	−12 – −10	5 min	7	600	Gentle
$ZnCl_2 \cdot H_2O$	R.T.	60 min	1 – 5	500	Moderate
$ZnCl_2/AlCl_3 \cdot 4H_2O$	R.T.	15 – 120 min	1 – 10	4080	Moderate
$ZnCl_2$/HCOOH/H_2O	R.T.	1.5 h	9	945	Moderate
Choline chloride: Imidazole	110	90 min	2.48	575	Moderate
$Ca(SCN)_2/H_2O$	120 – 140	20 – 40 min	1 – 5	1600	Gentle
H_2SO_4	−10 – 0	3 – 20 min	15 – 19	1230	Gentle

Table S4 Comparison of dissolution performance of this work with similar studies [32–39].

Solvent	Solvent temperature (°C)	Dissolution time	Solubility (wt.%)	Max DP	Moisture sensitivity
Tetrabutylammonium acetate/DMSO	R.T. – 40	2 min	8 – 15	1050	High
Tetrabutylphosphonium hydroxide/H_2O	R.T.	5 min	20	n.r.	Gentle
Tetrabutylammonium fluoride/DMSO	R.T.	15 min	2.5	650	High
Tetraethylammonium hydroxide /H_2O/urea	R.T.	60 min	15	1800	Gentle
Tetraoctylphosphonium acetate/DMSO	R.T.	10 – 20 min	8	500 – 1000	High
Methyltributylphosphonium acetate/DMSO	100 – 120	16 min	5 – 20	n.r.	High
Benzyltrimethylammonium hydroxide /H_2O	15 – 25	n.r.	3.1 – 6.8	n.r.	Gentle
Tetrabutylammonium acetate/N,N-dimethylacetamide	60	n.r.	9	n.r.	High

Note: n.r., not reported.

3 Conductivity of various TBAH solution

3.1 Conductivity of TBAH/DMSO solutions

Table S5 Electrical conductivity of TBAH/DMSO solvents prepared via evaporating TBAH/H_2O solution (Evap-H_2O–TBAH/DMSO) and TBAH/methanol/DMSO solution (Evap-MeOH–TBAH/DMSO), respectively. All measurements were conducted at room temperature (25 °C).

	Evap-H_2O–TBAH/DMSO	Evap-MeOH–TBAH/DMSO
Conductivity (mS/cm)	0.63	0.67

3.2 Conductivity of TBAH aqueous solution

For TBAH aqueous solution, 25 wt.% of TBAH (namely, 1.01 mol/L) showed the maximum κ of 78.6 mS/cm. The κ of TBAH aqueous solution was regulated by ion number when TBAH concentration was lower than 20 wt.%, and high concentration of TBAH (beyond 25 wt.%) led to the reduction of κ due to the enhancement of interionic electrostatic interactions.

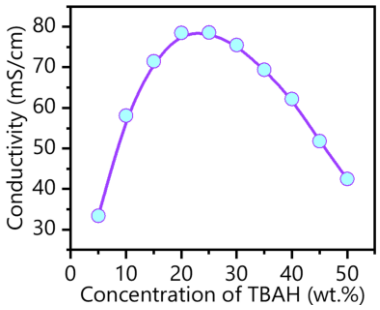

Figure S13 Conductivity of TBAH aqueous solution with different TBAH concentration.

4. Characterization of the interaction among TBAH, H_2O, DMSO, and cellulose

4.1 NMR spectra of cellobiose in different solvents

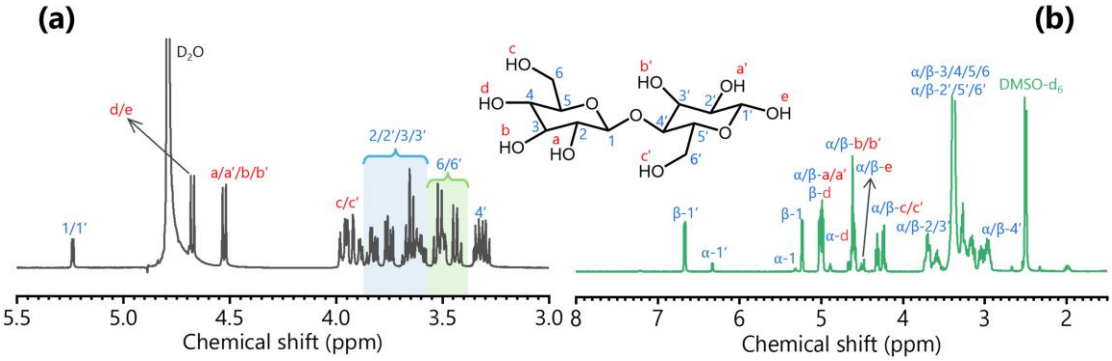

Figure S14 ^{1}H NMR spectra of cellobiose in different solvents. (a) D_2O; (b) DMSO-d_6.

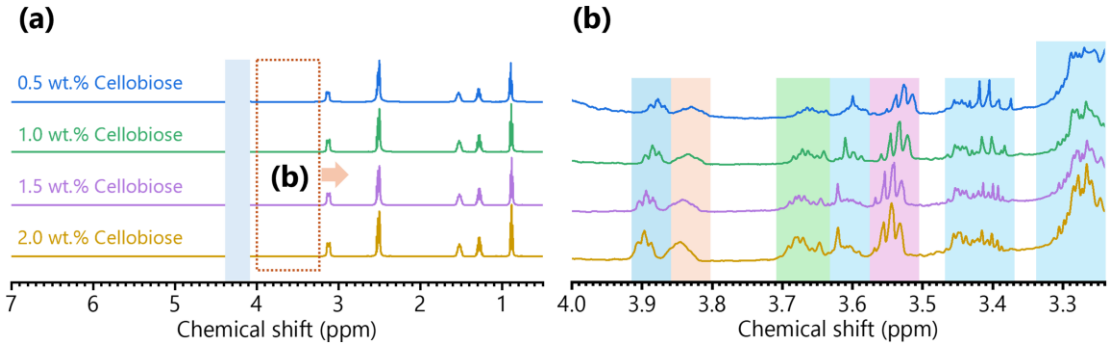

Figure S15 Overall (left) and magnified (right) ^{1}H NMR spectra of cellobiose in TBAH/H_2O/DMSO-d_6 by adjusting cellobiose concentration.

4.2 NMR spectra of cellulose in different solvents

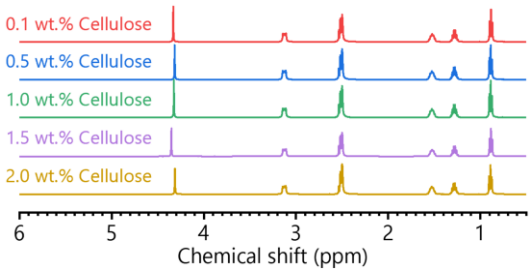

Figure S16 ^{1}H NMR spectra of cellulose in TBAH/H_2O/DMSO-d_6 by adjusting cellulose concentration.

5. Computer simulation of cellulose dissolved in TBAH/H_2O/DMSO

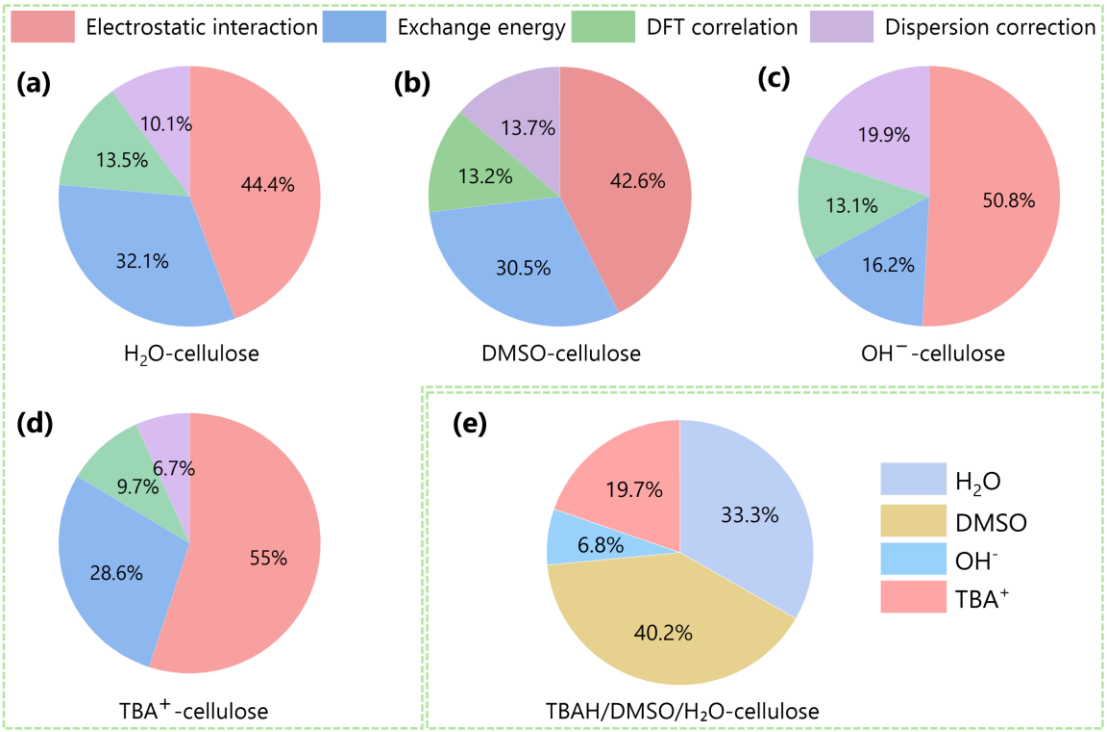

Figure S17 sobEDA interaction analysis between cellulose and TBAH/DMSO/H_2O solvent. (a-d) Fractional contributions of weak interactions (electrostatic interaction, exchange energy, DFT correlation, dispersion correction) between cellulose and H_2O (a), DMSO (b), OH^- (c), and TBA^+ (d), respectively; (e) Percentage contribution of H_2O, DMSO, OH^-, and TBA^+ to the total cellobiose–solvent interaction energy.

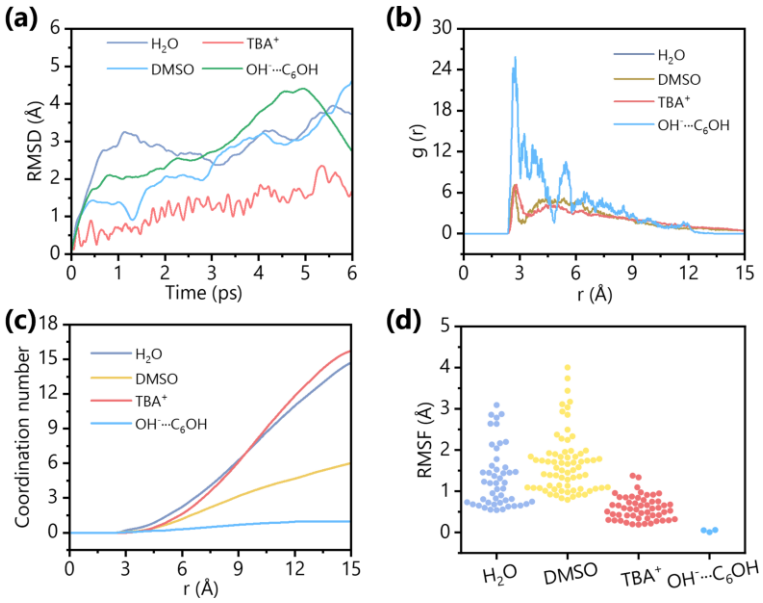

Figure S18 Molecular dynamics of cellulose dissolved in TBAH/DMSO/H_2O solvent. (a) RMSD curves of H_2O, DMSO, TBA^+, and $OH^-\cdots C_6OH$; (b) RDF curves of H_2O, DMSO, TBA^+, and $OH^-\cdots C_6OH$; (c) Coordination curves centered on H_2O, DMSO, TBA^+, and $OH^-\cdots C_6OH$, respectively; (d) RMSF plots of H_2O, DMSO, TBA^+, and $OH^-\cdots C_6OH$.

6. Fabrication and properties of the regenerated cellulose

6.1 Storage stability of cellulose solution

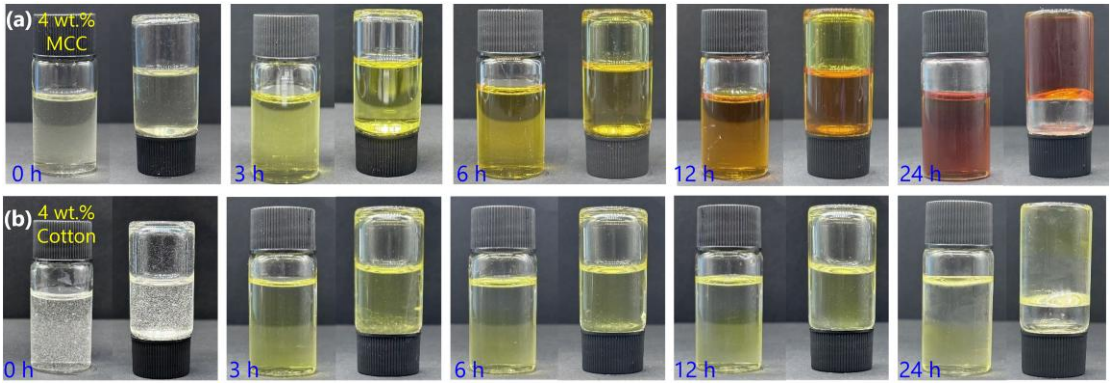

Figure S19 Digital images of (a) 4 wt.% MCC solution and (b) 4 wt.% cotton pulp solution standing for different durations.

6.1 Thermal stability of the regenerated cellulose

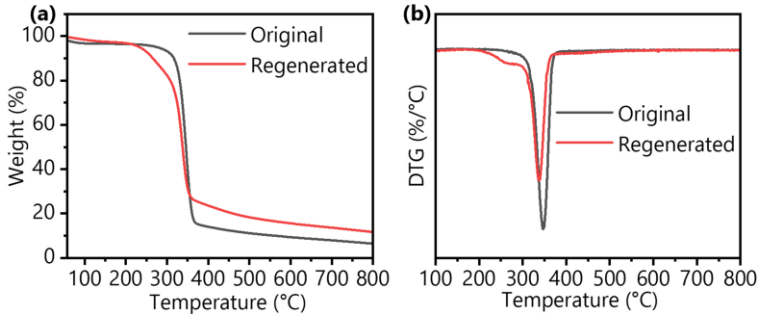

Figure S20 Thermogravimetric (TG) curves (a) and derivative thermogravimetry (DTG) curves (b) of MCC and the corresponding regenerated cellulose.

Both MCC and the corresponding regenerated cellulose showed minor weight loss below 100 °C. The main degradation of MCC and the corresponding regenerated cellulose occurred at 280 ~ 380 °C. The regenerated cellulose exhibited slightly lower degradation temperatures than MCC, which attributed to the reduced crystallinity.

6.2 Mechanical performance of the regenerated cellulose

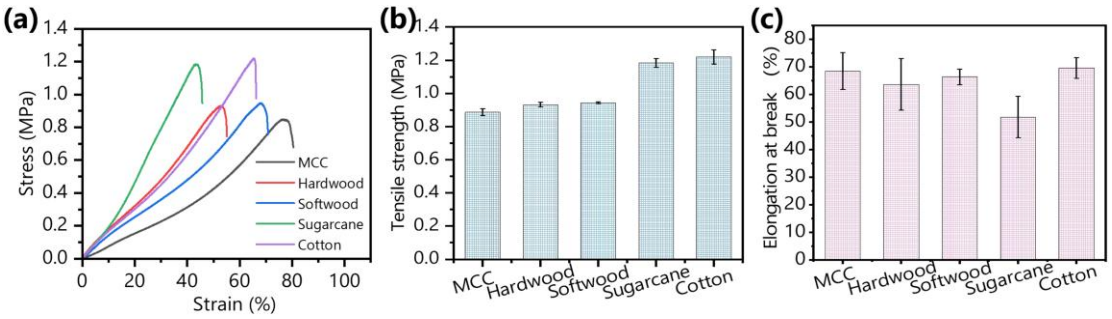

Figure S21 Tensile properties of the regenerated cellulose hydrogels. (a) Stress–strain curves; (b) Tensile strength; (c) Elongation at break.

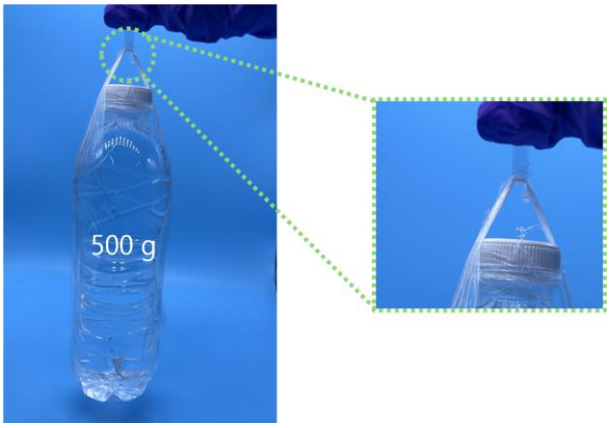

Figure S22 A digital image illustrating a regenerated cellulose strip (width: 5 mm) that suspended a 500 mL water bottle filled with water.

REFERENCES

1 H. Wang, B. Wang, S. Dong, Y. Yu, N. Wang and Z. Zhou, Diam. Relat. Mater., 2024, **149**, 111623.

2 D. A. Dolan, D. A. Sherman, R. Atkin and G. G. Warr, ChemPhysChem, 2016, **17**, 3096–3101.

3 L. Zhang, H. Yu, S. Liu, Y. Wang, T. Mu and Z. Xue, Ind. Eng. Chem. Res., 2023, **62**, 11723–11734.

4 M. J. Kamlet and R. W. Taft, J. Am. Chem. Soc., 1976, **98**, 377–383.

5 A. D. Becke, J. Chem. Phys., 1993, **98**, 5648–5652.

6 N. Barrios, J. G. Parra, P. Iza, R. A. Venditti and L. Pal, J. Phys. Chem. A, 2025, **129**, 5018–5033.

7 Z. Ju, Y. Yu, S. Feng, T. Lei, M. Zheng, L. Ding and M. Yu, Materials, 2022, **15**, 1158.

8 J. VandeVondele, M. Krack, F. Mohamed, M. Parrinello, T. Chassaing and J. Hutter, Comput. Phys. Commun., 2005, **167**, 103–128.

9 T. Lu and Q. Chen, Chemistry–Methods, 2021, **1**, 231–239.

10 T. Lu and F. Chen, J. Comput. Chem., 2012, **33**, 580–592.

11 Z. Tong, S. Zeng, H. Tang, W. Wang, Y. Sun, Q. Xia and H. Yu, Green Chem., 2023, **25**, 5086–5096.

12 W. Humphrey, A. Dalke and K. Schulten, J. Mol. Graph., 1996, **14**, 33–38.

13 T. D. Kühne, M. Iannuzzi, M. Del Ben, V. V. Rybkin, P. Seewald, F. Stein, T. Laino, R. Z. Khaliullin, O. Schütt, F. Schiffmann, D. Golze, J. Wilhelm, S. Chulkov, M. H. Bani-Hashemian, V. Weber, U. Borštnik, M. Taillefumier, A. S. Jakobovits, A. Lazzaro, H. Pabst, T. Müller, R. Schade, M. Guidon, S. Andermatt, N. Holmberg, G. K. Schenter, A. Hehn, A. Bussy, F. Belleflamme, G. Tabacchi, A. Glöß, M. Lass, I. Bethune, C. J. Mundy, C. Plessl, M. Watkins, J. VandeVondele, M. Krack and J. Hutter, J. Chem. Phys., 2020, **152**, 194103.

14 J. VandeVondele and J. Hutter, J. Chem. Phys., 2007, **127**, 114105.

15 J. VandeVondele and J. Hutter, J. Chem. Phys., 2003, **118**, 4365–4369.

16 S. Goedecker, M. Teter and J. Hutter, Phys. Rev. B, 1996, **54**, 1703–1710.

17 S. Grimme, J. Antony, S. Ehrlich and H. Krieg, J. Chem. Phys., 2010, **132**, 154104.

18 D. Van Der Spoel, E. Lindahl, B. Hess, G. Groenhof, A. E. Mark and H. J. C. Berendsen, J. Comput. Chem., 2005, **26**, 1701–1718.

19 M. J. Abraham, T. Murtola, R. Schulz, S. Páll, J. C. Smith, B. Hess and E. Lindahl, SoftwareX, 2015, **1–2**, 19–25.

20 Z. Liu, X. Sun, M. Hao, C. Huang, Z. Xue and T. Mu, Carbohydr. Polym., 2015, **117**, 99–105.

21 M. C. Jarvis, Cellulose, 2023, **30**, 667–687.

22 D. H. Brouwer and J. G. Mikolajewski, Cellulose, 2025, **32**, 4143–4160.

23 M. Akhlaghi Bagherjeri, H. Monhemi, A. N. M. A. Haque and M. Naebe, Carbohydr. Polym., 2024, **323**, 121433.

24 Y.-Y. Ma, Z.-L. Lu, Y.-Z. Xing, W.-S. Zheng and C.-G. Liu, Int. J. Biol. Macromol., 2024, **268**, 131729.

25 S. Rizvi and H. M. Gade, Biomass Bioenergy, 2025, **196**, 107758.

26 B. Xiong, P. Zhao, K. Hu, L. Zhang and G. Cheng, Cellulose, 2014, **21**, 1183–1192.

27 W. Ma, X. Li, L. Zhang, Y. Zheng, Y. Xi, J. Ma and Z. Wang, Int. J. Biol. Macromol., 2024, **272**, 132912.

28 Y. Xi, L. Zhang, Y. Tian, J. Song, J. Ma and Z. Wang, Green Chem., 2022, **24**, 885–897.

29 M. Hattori, T. Koga, Y. Shimaya and M. Saito, Polym. J., 1998, **30**, 43–48.

30 J. Shuai, X. Gao, J. Zhao, W. Ge, M. Tian, Z. Lei and X. Wang, Chem. Eng. J., 2024, **495**, 153280.

31 Z. Tong, S. Liu, H. Tang, J. Liu, W. Bi, Y. Liu, S. Zeng, Q. Xia, D. Zhao and H. Yu, Nano Lett., 2025, **25**, 14489–14496.

32 L. Sun, J. Han, C. Tang, J. Wu, S. Fang, Y. Li, Y. Mao, L. Wang and Y. Wang, Cellulose, 2022, **29**, 8133–8150.

33 A. J. Holding, A. Parviainen, I. Kilpeläinen, A. Soto, A. W. T. King and H. Rodríguez, RSC Adv., 2017, **7**, 17451–17461.

34 A. J. Holding, J. Xia, M. Hummel, H. Zwiers, M. Leskinen, D. Rico Del Cerro, S. Hietala, M. Nieger, M. Kemell, J. K. J. Helminen, V. Aseyev, H. Tenhu, I. Kilpeläinen and A. W. T. King, ChemPhysChem, 2022, **23**, e202100635.

35 J. Wu, Y. Zhong, H. Kang and R. Liu, Carbohydr. Polym., 2025, **352**, 123167.

36 M. Akhlaq and M. Uroos, J. Mol. Struct., 2025, **1327**, 141221.

37 R. Casarano, H. Nawaz, S. Possidonio, V. C. Da Silva and O. A. El Seoud, Carbohydr. Polym., 2011, **86**, 1395–1402.

38 M. Kostag, K. Jedvert, C. Achtel, T. Heinze and O. A. El Seoud, Molecules, 2018,

23, 511.

39 J. A. Sirviö and J. P. Heiskanen, Cellulose, 2020, **27**, 1933–1950.